Electronic Supplementary Material (ESI) for Nanoscale.

Supplementary Information

Construction of hetero-epitaxial nanostructure at the interface of Li-rich cathode materials to boost the rate capability and cycling performances

Jun Cao [a], Haijian Huang [a, b*], Yifan Qu [a], Weijian Tang[b], Zeheng Yang [a*], Weixin Zhang [a, b*]

[a] School of Chemistry and Chemical Engineering, Hefei University of Technology and Anhui Key Laboratory of Controllable Chemical Reaction & Material Chemical Engineering, 230009 Hefei, Anhui, PR China

[b] Institute of Energy, Hefei Comprehensive National Science Center, Hefei, Anhui 230071, P. R. China

* Corresponding authors

E-mail addresses: wxzhang@hfut.edu.cn; haijian.huang@hfut.edu.cn; zehengyang@hfut.edu.cn

Experimental Section

Synthesis of the Li-rich cathode material (LRMO):

A co-precipitation method was adopted to prepare the carbonate precursor ($Mn_{0.48}Ni_{0.24}Co_{0.08}(CO_3)_{0.8}$) of the lithium-rich cathode material. Typically, 4.8 mmol of $MnSO_4 \cdot H_2O$, 2.4 mmol of $NiSO_4 \cdot 6H_2O$ and 0.8 mmol of $CoSO_4 \cdot 7H_2O$ were dissolved in 30 mL distilled water. Meanwhile, 80 mmol $NaHCO_3$ were dissolved in 100 mL distilled water. The metal sulfate mixed solution was quickly poured into the $NaHCO_3$ solution and kept at room temperature under stirring for 3 h, which will lead to the formation of the MCO_3 (M= Mn, Ni, Co) precipitates. The wet precipitates were collected and rinsed by distilled water for 3 times and ethyl alcohol for 2 times, dried in air at 80 °C for 10 h to obtain the final carbonate precursor of $Mn_{0.48}Ni_{0.24}Co_{0.08}(CO_3)_{0.8}$. The carbonate precursor was then ground with a certain stoichiometric amount of Li_2CO_3 (5 % excess), calcined at 450 °C for 8 h and then 800 °C for 15 h at a heating rate of 2 °C min^{-1}, and the Li-rich cathode material can be eventually obtained.

Synthesis of the lithiated transition metal phosphates ($LiMPO_4$) coated LRMO (LRMO@$LiMPO_4$):

Typically, 1 g of the carbonate precursor was first dispersed in 100 mL water-ethylene glycol mixed solution (1:5 in volume) and ultrasonicated to obtain the uniformly dispersed mixture. Afterwards, different amounts of NaH_2PO_4 (0.021 g, 0.042 g, 0.063 g) were dissolved in the mixture under stirring. The etching reaction will take place at this stage, which was kept at 60°C for 5 h. Next, the precipitate was collected and rinsed thoroughly with deionized water and absolute ethanol. The wet powder was dried in an oven at 80°C for 10 h and then fully ground with a certain stoichiometric amount of Li_2CO_3 (5% excess). The obtained mixture powder was pre-heated at 450 °C for 8 h, and then at 800°C for 15 h to obtain the final LRMO@$LiMPO_4$.

Evaluation of the pH evolution:

0.6 g of the carbonate precursors were dispersed into 10 mL deionized water. Next, either 50 mL deionized water or 50 mL EG were added into the above mixture, forming two dispersions. After stirring, 0.1 mmol of NaH_2PO_4 were added into the above two dispersions. The changes of the pH values with time for the obtained two dispersions were recorded using a pH meter.

Physical Characterizations:

The X-ray diffraction (XRD) measurements were conducted on a Rigaku XRD instrument (Rint-2000) with Cu-Kα radiation (λ= 0.154178 nm), operated at 40 kV and 80 mA. Raman spectra were collected on a LabRam HR Evolution instrument. The field-emission scanning electron microscopy (FESEM) and transmission electron microscopy (TEM) images were acquired on a Hitachi SU8020 FESEM equipped with an energy dispersive spectrometer (EDS) and a JEOL-2010 TEM instrument, respectively. X-ray photoelectron spectroscopy (XPS) spectra were obtained on Thermo ESCALAB250Xi with Al Ka radiation as the excitation source, where the binding energy was calibrated taking C 1s = 284.8 eV.

Electrochemical measurements:

The electrochemical properties of LRMO and LRMO@$LiMPO_4$ were analyzed using

2032-type coin cells assembled in an argon-filled glove box (LABstar, Germany, MBRAUN). The active material (80 wt%) was mixed with polyvinylidene fluoride (10 wt%) and acetylene black (10 wt%) in the solvent of N-methylpyrrolidinone (NMP) to form a homogeneous slurry, which was coated onto the current collector of Al foils. The wet electrodes containing NMP were dried at 80°C for 12 h under vacuum. The coin cells were then assembled using the as-obtained electrode as the cathode, the Li foil as the anode, the Celgard 2400 membrane as the separator, and 1 M $LiPF_6$ dissolved in ethylene carbonate (EC)/dimethyl carbonate (DMC)/ethyl methyl carbonate (EMC) (1:1:1 by volume) as the electrolyte. The battery performances were evaluated at room temperature using the Newware Battery Test System. The cyclic voltammetry (CV) measurements and the electrochemical impedance spectroscopy (EIS) measurements were both performed on a CHI660D (CH instruments Co., Ltd., Shanghai, China) electrochemical workstation. The CV curves were collected at 0.1 mVs^{-1} within the voltage range of 2.0-4.8 V.

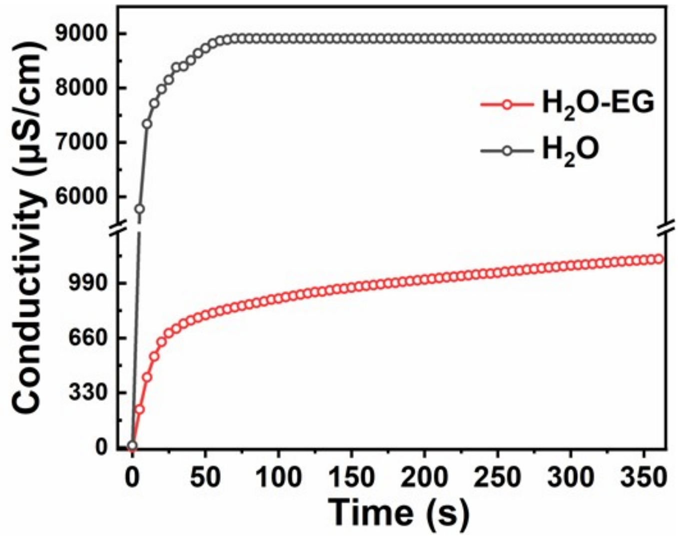

Fig. S1. The ionic conductivity evolution of the NaH_2PO_4 solutions in different solvents.

The mixed solvent (H_2O-EG), acting as the reaction medium, plays a crucial role in realizing the uniform coating of $LiMPO_4$. To demonstrate this, 1 mmol NaH_2PO_4 was gradually added into 50 mL of the mixed H_2O-EG solvent (Solution A) and pure water (Solution B), respectively, and the ionic conductivities of the two solutions were measured. As shown in Fig. S1, the ionic conductivity for Solution A is found to scale up much slower than that for the control solution of Solution B. The results suggest that the mixed solvent can retard the ionization of NaH_2PO_4 to a large extent.

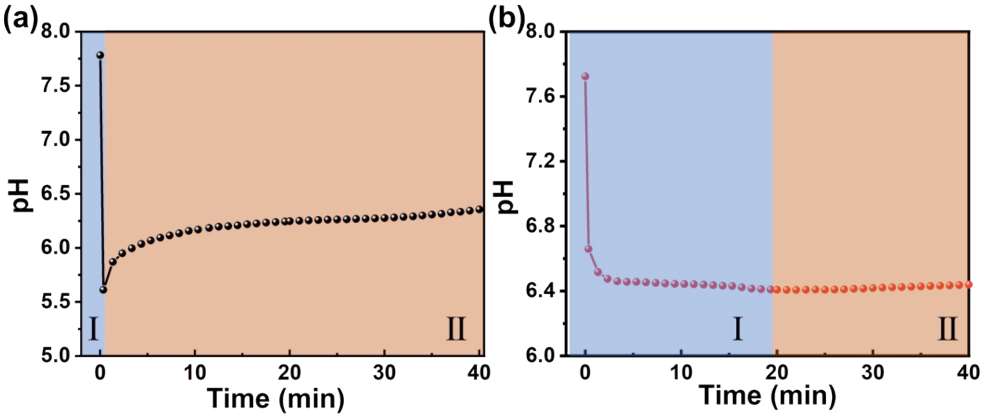

Fig. S2. The pH evolution of the mixture of (a) the carbonate precursor and NaH_2PO_4 dissolved in pure water and (b) the carbonate precursor and NaH_2PO_4 dissolved in pure water/EG.

A certain amount of the carbonate precursors was added into the two solutions described in Fig. S1, while the pH evolution of the two dispersions with time was recorded. Due to the generation of H^+ during the ionization of NaH_2PO_4, the pH values for both dispersions are observed to decrease during the initial step (step I). However, for the carbonate precursors dissolved in Solution B, the pH value drops much more sharply from 7.781 to 5.612 within a very short time (Fig. S2a). For comparison, the pH of the carbonate precursor dispersion in Solution A decreases from 7.723 to 6.659 at a relatively much more moderate rate (Fig. S2b). According to the above results, NaH_2PO_4 is more liable to be ionized and to release H^+ in water than in the H_2O-EG system. Consequently, the more acidic solution in the pure water system will provoke fast etching of the carbonate precursor MCO_3, as reflected by the fast increase of the pH value in the following procedure (Step II, see Fig. S2a). In such a case, the nucleation speed of the transition metal phosphates is not easy to be under control, based on which the homogeneous coating of NaH_2PO_4 on LRMO becomes difficult. In contrast, for the H_2O-EG system, the more moderate pH evolution offers a mild environment for the etching reaction to take place, which leads to the homogeneous growth of the metal phosphate on LRMO at a slow rate during step II (Fig. S2b).

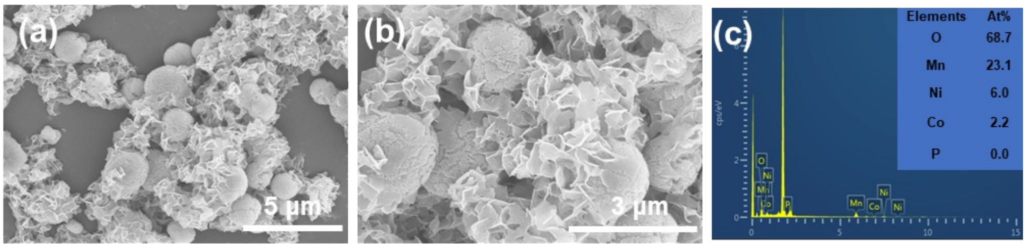

Elements	At%
O	68.7
Mn	23.1
Ni	6.0
Co	2.2
P	0.0

Fig. S3. (a, b) SEM images and (c) the corresponding EDS spectrum of the obtained samples using pure water as the solvent.

According to the analysis in Fig. 2a-2c, NaH_2PO_4 is more liable to be ionized and to release H^+ in water than in the H_2O-EG system. Consequently, the more acidic solution in the pure water system will provoke fast etching of the carbonate precursor MCO_3. In such a case, the nucleation speed of the transition metal phosphates is not easy to be under control, based on which the homogeneous coating of NaH_2PO_4 on LRMO becomes difficult. As evidence, separate coating particles, instead of a uniform coating layer, were observed when using pure water as the solvent (Fig. S3).

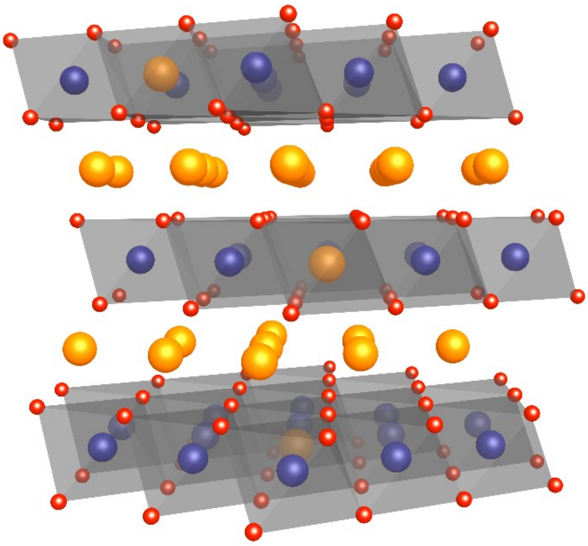

Fig. S4. Structural model of LRMO

For the Li-rich layered structure, the TM ions are located at the 3b octahedron sites, while the Li^+ ions occupy the 3a tetrahedron sites. Meanwhile, there are a small portion of Li^+ ions that are located at the 3b octahedron sites in the TM layer, as shown in Fig. S4.

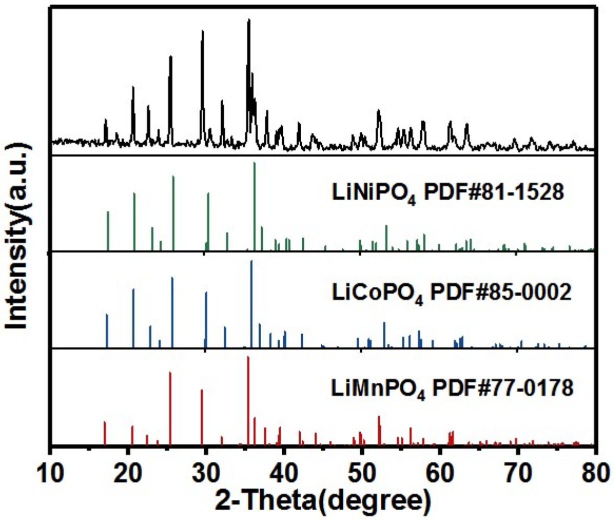

Fig. S5. XRD patterns of the annealed $M_3(PO_4)_2$ (M=Ni, Co, and Mn)

To verify that the intermediate product of $M_3(PO_4)_2$ in the coating layer are also transferred into lithiated $LiMPO_4$ during the Li-implanting process, $M_3(PO_4)_2$ was mixed with Li_2CO_3 and underwent the same lithiation procedure as that for the synthesis of LRMO@$LiMPO_4$. Here, $M_3(PO_4)_2$ was synthesized based on the reaction of NaH_2PO_4 with MSO_4 in the mixed solvent of H_2O-EG (see experimental section). As shown in Fig. S5, the XRD patterns of the annealed samples are well in line with the characteristics of $LiMnPO_4$, $LiCoPO_4$ and $LiNiPO_4$, respectively, which indicates the lithiation of transition metal phosphates during the Li-implanting procedure.

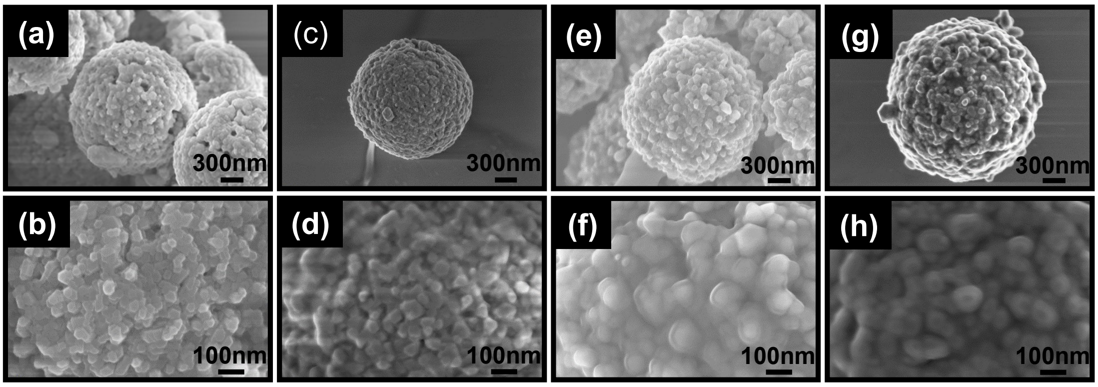

Fig. S6. SEM images of (a, b) LRMO, (c, d) LRMO@LiMPO$_4$-1, (e, f) LRMO@LiMPO$_4$-2, and (g, h) LRMO@LiMPO$_4$-3.

The SEM images of the pristine LRMO sample and the coated samples demonstrate that all the four samples exhibit porous spherical morphology with a diameter of around 2 μm (Fig. S6). The porous structures can be due the generation of CO_2 during the decomposition of the carbonate precursors.

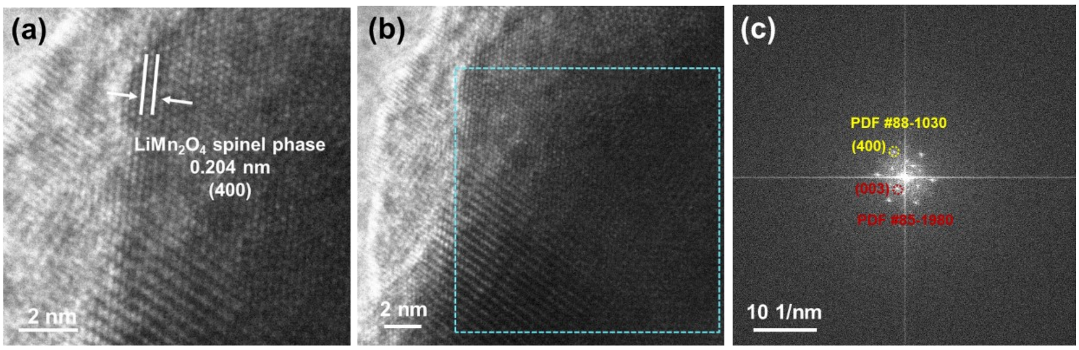

Fig. S7. (a, b) HRTEM images of LRMO@LiMPO_4-2 and the corresponding FFT patterns of the selected area in Fig. S7b.

Fig. S7 illustrates the existence of the $LiMn_2O_4$ spinel phase in the core area, which is in line with the Raman results as discussed in the main text. Besides, FFT analysis of the selected area in the HRTEM image (Fig. S7a) was further performed. Evaluation of the FFT results points to (400) reflection of the spinel-type $LiMn_2O_4$ (PDF #88-1030) and (003) reflection of LRMO (PDF #85-1980), further confirming the existence of the spinel phase in the structure.

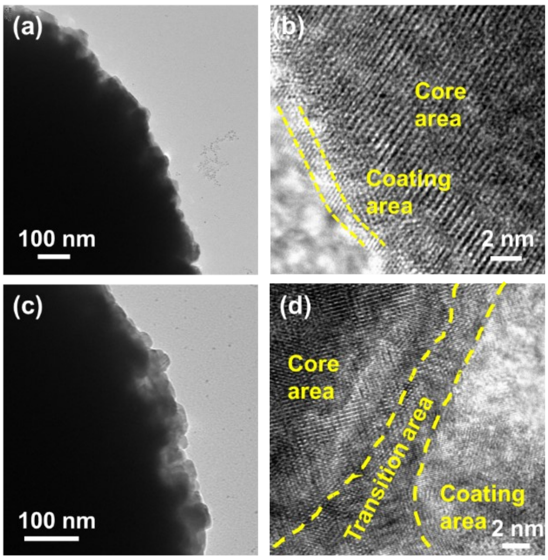

Fig. S8. TEM images of (a) LRMO@LiMPO_4-1 and (c) LRMO@LiMPO_4-3. HRTEM images of (b) LRMO@LiMPO_4-1 and (d) LRMO@LiMPO_4-3.

The LRMO@LiMPO_4-1 sample show similar morphological features as that of LRMO@LiMPO_4-2, except that the coating layer of the former sample is much thinner than that of the latter one (Fig. S8). However, for the LRMO@LiMPO_4-3 sample, an obvious transition area is observed at the interface, with the hetero-epitaxial structure nearly disappearing (Fig. S8). The results can be likely induced by the larger content of the coating specie in LNCM-3, which gives rise to the higher degree of PO_4^{3-} doping in LRMO that damages the interfacial structure.

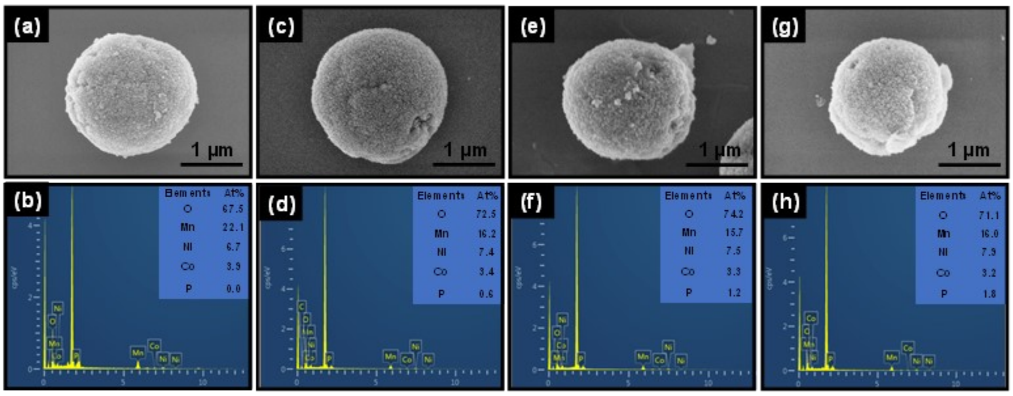

(b)

Elements	At%
O	67.5
Mn	22.1
Ni	6.7
Co	3.9
P	0.0

(d)

Elements	At%
O	72.5
Mn	16.2
Ni	7.4
Co	3.4
P	0.6

(f)

Elements	At%
O	74.2
Mn	15.7
Ni	7.5
Co	3.3
P	1.2

(h)

Elements	At%
O	71.1
Mn	16.0
Ni	7.9
Co	3.2
P	1.8

Fig. S9. SEM images and the corresponding EDS spectra of (a, b) LRMO, (c, d) LRMO@LiMPO$_4$-1, (e, f) LRMO@LiMPO$_4$-2, and (g, h) LRMO@LiMPO$_4$-3.

The energy dispersive spectroscopy (EDS) results reveal the uniform distribution of O, Mn, Ni, Co, and P within the composite particles, attesting to the homogeneous coating of LiMPO$_4$ on LRMO (Fig. S9).

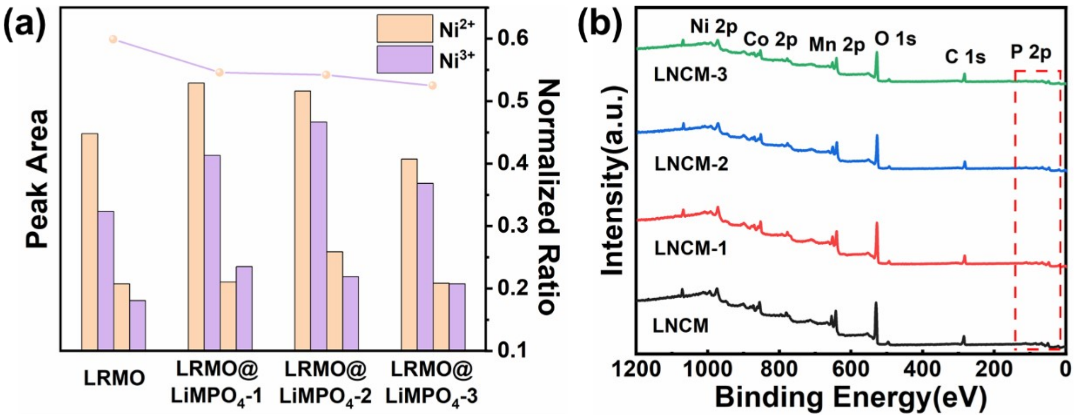

Fig. S10. (a) Peak areas of Ni^{2+} and Ni^{3+} for LRMO and the coated samples. (b) XPS Full spectra for LRMO and the coated samples.

The Ni 2p spectra of LRMO and LRMO@$LiMPO_4$-2 reveals that the intensity ratios of Ni^{3+}/Ni^{2+} are higher in the coated samples relative to the pristine one (Fig. S10). The results can be ascribed to the doping of PO_4^{3-}, which inevitably increases the average valence state of Ni on basis of charge balance. The appearance of the P XPS signal in the coated samples further corroborates the successful $LiMPO_4$ coating on the surface of LRMO (Fig. S10).

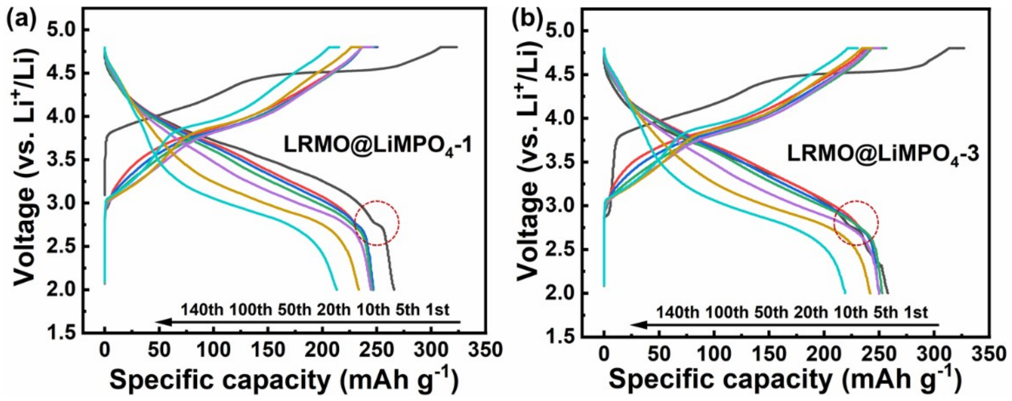

Fig. S11. Charge-discharge profiles of (a) LRMO@LiMPO$_4$-1 and (b) LRMO@LiMPO$_4$-3

Fig. 5a, 5b and Fig. S11 present the charge-discharge profiles of LRMO and the coated samples. According to the results, the initial Coulombic efficiencies of LRMO@LiMPO$_4$-, LRMO@LiMPO$_4$-2, and LRMO@LiMPO$_4$-3 are determined to be about 82.1%, 82.6%, and 78.8%, respectively, which are all higher than 76.8% achieved for the primary LRMO. Besides, a small discharge plateau at around 2.7 V (as marked by the small circle in Fig. 5a and Fig. S11) are observed for the coated samples, which is absent in that of the pristine LRMO sample. Such a discharge plateau can be related to the redox reaction of the spinel phase, which only exists in the coated samples.

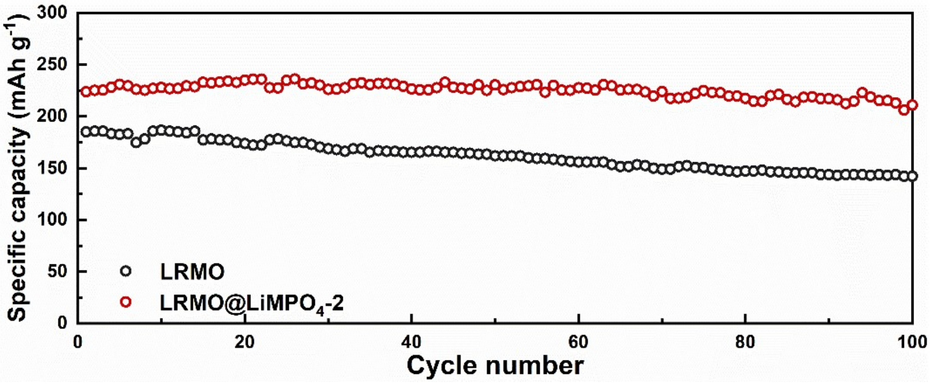

Fig. S12. Cycling performances of the pristine LRMO and LRMO@LiMPO$_4$-2 at 1 C.

When evaluated at a higher rate of 1 C after 100 cycles, LRMO could still deliver a discharge capacity of 194.9 mAh g^{-1}, corresponding to 77.2% of the initial capacity (Fig. S12). For comparison, LRMO@LiMPO$_4$-2 achieves a much higher discharge capacity of 213.6 mAh g^{-1} that represents 91.0% of the initial capacity, further evidencing the outstanding cycling performance of the coated LRMO@LiMPO$_4$-2 sample.

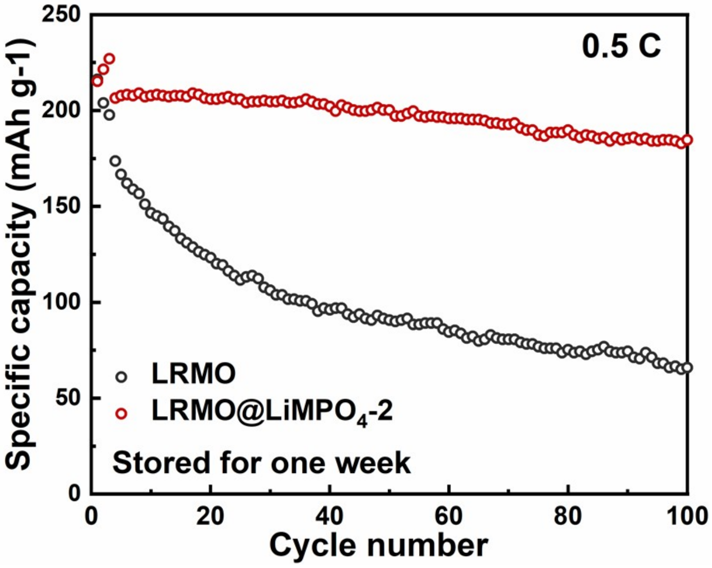

Fig. S13. Cycling performances at 0.5 C for the pristine LRMO and LRMO@LiMPO$_4$-2 collected after being stored in a dryer for one week.

To probe into the influences of the LiMPO$_4$ coating layer on reducing the residual alkali, the pristine sample and the coated sample were both stored in the ambient atmosphere for a week prior to the performance evaluation. As shown in Fig. S13, LRMO@LiMPO$_4$-2 exhibits a similar cycling performance as that of the fresh sample, with a capacity retention of 88.5% achieved after 100 cycles. However, for the pristine sample, the capacity retention drops significantly to 37.9% after 100 cycles at 0.5 C.

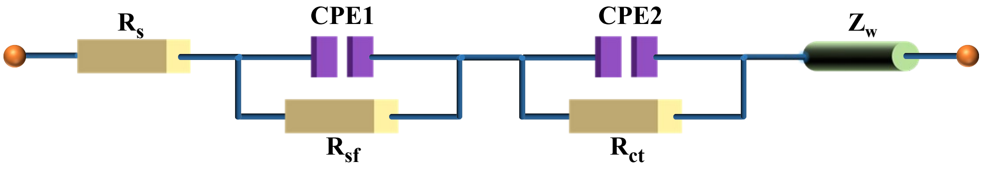

Fig. S14. The equivalent circuit of the EIS spectra in Fig. 6c

Table S1. Rietveld refinement results for the cell parameters of the samples

Sample	**a(Å)**	**c(Å)**	**c/a**	**V (Å^3)**	**I_{003}/I_{104}**
LNCM	2.8405	14.2098	5.0026	99.2877	1.5830
LNCM-1	2.8484	14.2493	5.0026	100.1183	1.6416
LNCM-2	2.8511	14.2592	5.0013	100.3779	1.7094
LNCM-3	2.8554	14.2650	4.9958	100.7218	1.8045

The analysis of the lattice parameters for the four samples (Table S1) uncovers that the crystal structure of the as-obtained LRMO samples is influenced, to some extent, by the feeding ratios of NaH_2PO_4 during synthesis. Specifically, with more NaH_2PO_4 being added during synthesis, a larger *c*-lattice parameter is found. The results implicate the slightly increase of the Li-layer distance in the structure, which can be likely ascribed to the possible occurrence of PO_4^{3-} doping in LRMO when a larger amount of NaH_2PO_4 is introduced during synthesis. Note that the doping process involves the replacement of O^{2-} in the structure by tetrahedral PO_4^{3-} that possesses a much larger ionic radius than the O^{2-} anions, which lead to the expansion of the Li-layer. The expanded Li-layer will benefit the fast Li-ion extraction/intercalation processes.

Table S2. Electrochemical performances of LRMO, LRMO@ $LiMPO_4$-1, LRMO@ $LiMPO_4$-2, and LRMO@ $LiMPO_4$-3

Samples	**Initial Coulombic Efficiency**	**Rate performance (mAh g)**						**Capacity Retention (after 140 cycles at 0.5C)**
		0.1 C	**0.2 C**	**0.5 C**	**1 C**	**2 C**	**5 C**	
LRMO	76.8%	281.2	232.4	205.9	180.6	148.8	107.4	78.0%
LRMO @$LiMPO_4$-1	82.1%	251.2	252.7	235.2	219.1	187.8	140.5	85.3
LRMO @$LiMPO_4$-2	82.6%	269.3	271.0	252.4	235.5	210.7	159.3	93.4%
LRMO @$LiMPO_4$-3	78.6%	223.9	230.2	233.3	216.7	196.8	156.3	86.9%